Severity and Consolidation Quantification of COVID-19 From CT Images Using Deep Learning Based on Hybrid Weak Labels

Dufan Wu ⓘ, Kuang Gong ⓘ, Chiara Daniela Arru, Fatemeh Homayounieh, Bernardo Bizzo ⓘ,
Varun Buch, Hui Ren, Kyungsang Kim ⓘ, Nir Neumark ⓘ, Pengcheng Xu, Zhiyuan Liu, Wei Fang,
Nuobei Xie, Won Young Tak, Soo Young Park, Yu Rim Lee, Min Kyu Kang, Jung Gil Park,
Alessandro Carriero, Luca Saba, Mahsa Masjedi, Hamidreza Talari, Rosa Babaei, Hadi Karimi Mobin,
Shadi Ebrahimian, Ittai Dayan, Mannudeep K. Kalra, and Quanzheng Li ⓘ

Abstract—Early and accurate diagnosis of Coronavirus disease (COVID-19) is essential for patient isolation and contact tracing so that the spread of infection can be limited. Computed tomography (CT) can provide important information in COVID-19, especially for patients with moderate to severe disease as well as those with worsening cardiopulmonary status. As an automatic tool, deep learning methods can be utilized to perform semantic segmentation of affected lung regions, which is important to establish disease severity and prognosis prediction. Both the extent and type of pulmonary opacities help assess disease severity. However, manually pixel-level multi-class labelling is time-consuming, subjective, and non-quantitative. In this article, we proposed a hybrid weak label-based deep learning method that utilize both the manually annotated pulmonary opacities from COVID-19 pneumonia and the patient-level disease-type information available from the clinical report. A UNet was firstly trained with semantic labels to segment the total infected region. It was used to initialize another UNet, which was trained to segment the consolidations with patient-level information using the Expectation-Maximization (EM) algorithm. To demonstrate the performance of the proposed method, multi-institutional CT datasets from Iran, Italy, South Korea, and the United States were utilized. Results show that our proposed method can predict the infected regions as well as the consolidation regions with good correlation to human annotation.

Index Terms—Computed tomography, COVID-19, segmentation, lung, deep learning, severity, consolidation, weak label.

Dufan Wu, Kuang Gong, Chiara Daniela Arru, Fatemeh Homayounieh, Hui Ren, Kyungsang Kim, Pengcheng Xu, Zhiyuan Liu, Wei Fang, Nuobei Xie, Shadi Ebrahimian, Mannudeep K. Kalra, and Quanzheng Li are with the Department of Radiology, Massachusetts General Hospital, Boston, MA 02114 USA (e-mail: dwu6@mgh.harvard.edu; kgong@ mgh.harvard.edu; carru@mgh.harvard.edu; fhomayounieh@mgh. harvard.edu; hren2@mgh.harvard.edu; kkim24@mgh.harvard.edu; pxu3@mgh.harvard.edu; zliu40@mgh.harvard.edu; wfang3@mgh. harvard.edu; nxie@mgh.harvard.edu; sebrahimian@mgh.harvard.edu; mkalra@mgh.harvard.edu; quanzheng@mgh.harvard.edu).

Bernardo Bizzo, Varun Buch, Nir Neumark, and Ittai Dayan are with the MGH & BWH Center for Clinical Data Science, Boston, MA 02114 USA (e-mail: bbizzo@mgh.harvard.edu; varun.buch@mgh. harvard.edu; nir.neumark@mgh.harvard.edu; idayan@partners.org).

Won Young Tak, Soo Young Park, and Yu Rim Lee are with the Department of Internal Medicine, School of Medicine, Kyungpook National University, Daegu 41944, South Korea (e-mail: wytak@knu.ac.kr; psy@knu.ac.kr; deblue00@naver.com).

Min Kyu Kang and Jung Gil Park are with the Department of Internal Medicine, Yeungnam University College of Medicine, Daegu 41944, South Korea (e-mail: kmggood111@naver.com; jgpark@ynu.ac.kr).

Alessandro Carriero is with the Radiologia, Azienda Ospedaliera Universitaria Maggiore della Carità, 28100 Novara, Italy (e-mail: profcarriero@virgilio.it).

Luca Saba is with the Radiologia, Azienda Ospedaliera Universitaria Policlinico di Cagliari, 09124 Cagliari, Italy (e-mail: lucasabamd@gmail.com).

Mahsa Masjedi and Hamidreza Talari are with the Department of Radiology, Shahid Beheshti Hospital, Kashan 00000, Iran (e-mail: mahsami141@gmail.com).

Rosa Babaei and Hadi Karimi Mobin are with the Department of Radiology, Firoozgar Hospital, Iran University of Medical Sciences, Tehran 48711-15937, Iran (e-mail: rosa.babaei@gmail.com; hadi.karimimobin@gmail.com).

Digital Object Identifier 10.1109/JBHI.2020.3030224

I. INTRODUCTION

SINCE November 2019, coronavirus disease 2019 (COVID-19) has in total 7.1 million confirmed cases and caused 363,000 deaths worldwide as of June 6th, 2020 [1]. Symptoms of COVID-19 include fever, cough, fatigue, with 17% to 29% of the patients showing acute respiratory distress syndromes (ARDS) [2]. Due to its high contagiousness (reproductive number = 3.28 [3]), early diagnosis of COVID-19 is critical so that mitigating steps such as patient isolation and contract tracing can be enforced to limit spread, and supportive treatment can be initiated. Reverse-transcription polymerase chain reaction (RT-PCR) assay is the gold standard for COVID-19 diagnosis. In early phase of infection (4-10 days), RT-PCR assays have low sensitivity (60-70%), which increases substantially over time [4]–[6]. Although initial studies suggested a sensitivity as high as 98% for computed tomography (CT) [5], later studies reported that about 18% of non-severe COVID-19 pneumonia have no imaging findings [7]. Per the prestigious Fleischner Society recommendations, chest CT is not indicted for mild COVID-19

infection but provides useful information in patients with moderate to severe disease as well as in those with worsening pulmonary functions [8]. Compared to RT-PCR, CT provides more information on the confirmed patients, e.g., the severity of their lung infection, the progression of the disease, and any complications such as the myocardial injury [9]. Relevant information is crucial for patient management and making treatment planning. Early CT imaging characteristics of COVID-19 are usually bilateral peripheral focal or multifocal ground-glass opacities (GGO). Crazy-paving patterns (GGO with superimposed inter- and intralobular septal thickening) and consolidation become the dominant CT findings in advanced or more severe disease forms [6], [10]–[12].

Prior studies have reported subjective grading of CT images by radiologists to calculate the severity score of COVID-19 pneumonia based on the type of pulmonary opacities (such as GGO, crazing paving pattern, or consolidation) and the extent of involvement of each lung lobe (based on visual perception of percentage of lung lobe involved) to assess disease severity and disease progression. However, such scoring system is inefficient, not part of standard diagnostic interpretation, and prone to inter- and intra-observer variations. For example, up to 25% lobar involvement is given a score of 2 and 26% lobar involvement gets a score of 3 for extent of opacities – such arbitrary classification is extremely challenging and inconsistent with visual or qualitative interpretation. Thus, developing an automated tool to quantify the severity of COVID-19 based on CT images is an urgent and unmet need to enhance diagnostic information and augment its prognostic value. [13].

With the initial success on computer vision tasks [14], deep learning methods have been widely applied to various medical imaging areas, e.g., denoising, reconstruction, detection, and segmentation. As for COVID-19 diagnosis, several groups have performed pioneering studies showing that deep learning can accurately detect COVID-19 and differentiate it from other lung disease [15]–[22]. Apart from COVID-19 diagnosis, semantic segmentation of the infected lung regions is crucial as it is a tool for further quantitative disease monitoring [23]. Deep learning methods have also been applied to COVID-19 CT image segmentation. Specifically, Huang *et al.* [23] have developed a segmentation network to perform serial quantitative CT assessment of Covid-19. Shan *et al.* [24] have devised a human-in-the-loop strategy during network training to reduce the manual labelling efforts. Chaganti *et al.* [25] has designed a deep learning pipeline to perform semantic segmentation and various severity measures together. Based on the semantic segmentation developed, assessment of features extracted from the infection regions can be used for further disease prediction [26], [27].

Most of the existing method focuses on segmenting the total infected areas without discriminating between GGO and consolidation. Chaganti *et al.* [25] used a threshold of -200 HU to separate consolidation from the predicted infected regions. Fan *et al.* [28] proposed a semi-supervised learning method to combine limited semantic annotations of consolidation with CT images not labeled for consolidation. In [28], a network was initially trained on a small set of images with consolidation annotations. The network was progressively tested on unlabeled CT images which was then included in the training dataset. Here we explored a different training strategy compared to [28], where only image-level labels for consolidation were used. Several noticeable methods have been proposed for weakly labeled segmentation, including multi-instance learning [29], localization maps [30], and expectation maximization (EM) [31], [32]. We employed the EM framework in this work because of its ability to easily incorporate prior functions on the target area.

In this work, we proposed a deep learning approach to learn the infection and consolidation information from CT images based on hybrid weak labels: patient-level multi-class information and manually labelled infection contours. A UNet was first trained with supervised learning to predict the infected regions based on strong semantic labels. Then it was fine-tuned to predict the consolidation regions based on patient-level labels only using EM algorithm. Since consolidation usually has higher Hounsfield unit (HU), a prior function was proposed to model the probability of a pixel being consolidation. The model was trained on CT images from Iran and validated on images from various datasets from Iran, Italy, South Korea, the United States and MedSeg.

Compared to existing studies, the main contributions of this work are as follows: (1) The EM algorithm was applied for weakly supervised learning of the segmentation of consolidation in COVID-19 CT datasets. Compared to the progressive learning framework [28], the proposed method does not need any starting semantic labels for the consolidation; (2) A novel prior function was proposed to model the consolidation in lung, which combined the data-driven network training with the expert-knowledge modeling; (3) More detailed derivation of the EM learning algorithm were derived compared to [31], which will be given in the appendix.

This paper is organized as follows. Section II introduces the proposed framework and implementation details. Experiment set-up and dataset details are presented in section III. Experimental results are shown in section IV, followed by discussions in section V. Finally, conclusions are drawn in Section VI.

II. METHODOLOGY

A. Overview

The proposed deep learning method[1] consisted of the following two steps:

Step 1: training a semantic segmentation network for infected lung regions based on strong label.

Step 2: training a semantic segmentation network for consolidation based on patient-level weak label.

In step 1, a 2D UNet [33] was employed to segment the infection regions from the CT images (UNet-1). The training labels were CT images with pixel-level annotation of being infected or not. In step 2, UNet-1 was further finetuned to segment consolidation from the infected regions (UNet-2). A subset of the training images was annotated regarding the existence of consolidation for each patient. The consolidation network was trained in the framework of EM [31] to learn the segmentation of consolidation from patient-level annotations. A flowchart of the entire training process is given in Fig. 1.

---

[1]Code available at: https://github.com/wudufan/lung_seg_em
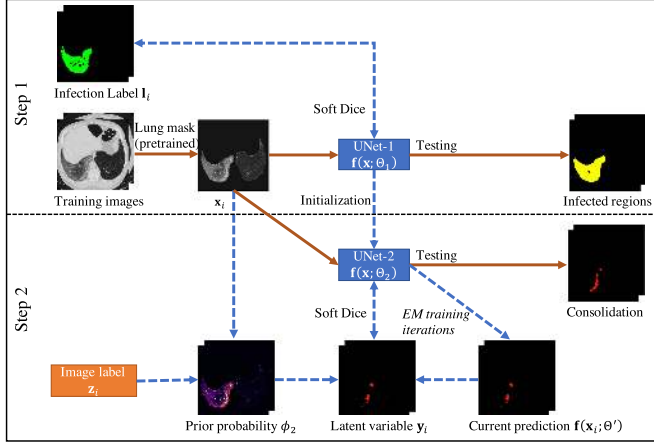
Fig. 1. Flowchart of the proposed hybrid label learning. Step 1 trains the infected region segmentation network UNet-1 using fully supervised learning. UNet-1 also provides initialization for the consolidation segmentation network UNet-2. Step 2 trains UNet-2 combining the image-level label $\mathbf{z}_i$ and prior probability ϕ_2 built from images $\mathbf{x}_i$. The solid brown lines are the procedures that are involved in both training and testing, whereas the dashed blue lines are training procedures only.

UNet-1 and UNet-2 had identical structures with 1-channel output activated by Sigmoid function. Both took 7 adjacent CT slices as input and output a two-class segmentation of the central slice. They used the standard UNet structure [33] and detailed parameters will be introduced in section III-B. To make the network concentrate on features inside the lung only, the lung masks were generated by a pretrained lung segmentation network [34] and applied to the CT images before being fed into the UNets.

B. Segmentation of the Infected Region With Strong Labels

We used 2D UNet with smooth Dice loss[2] to learn the segmentation of infected regions. Denote the semantic label of the training image i as $\mathbf{l}_i \in \{0,1\}^J$, where J is the number of pixels in the labels. For pixel j, we have:

$$l_{ij} = \begin{cases} 1, & \text{Infected} \\ 0, & \text{Not infected} \end{cases}. \tag{1}$$

Denote UNet-1 as $\mathbf{f}(\mathbf{x}_i; \Theta)$ where $\mathbf{x}_i$ is the ith training image and Θ is the network parameters to be learned. The Dice loss was employed for the training as:

$$\Theta_1 = \arg \min_{\Theta} -\frac{1}{N} \sum_i \frac{2\mathbf{l}_i \cdot \mathbf{f}(\mathbf{x}_i; \Theta) + \sigma}{\|\mathbf{l}_i\|_1 + \|\mathbf{f}(\mathbf{x}_i; \Theta)\|_1 + \sigma}, \tag{2}$$

where N is the number of training images and σ is the smoothing parameter which was set to 1 based on experience. After Θ was learned, a binary segmentation of the infected regions was given for each image $\mathbf{x}$ where pixel j was infected if $\mathbf{f}(\mathbf{x}; \Theta_1)_j > 0.5$.

C. EM Framework for Weak Label Segmentation

We employed the EM framework [31] to solve the weakly labeled segmentation problem. Denote UNet-2 as $\mathbf{f}(\mathbf{x}_i; \Theta)$, which

[2]https://github.com/jocicmarko/ultrasound-nerve-segmentation

outputs the probability of each pixel belonging to consolidation. Denoting the image-level annotation as z_i for image i, where:

$$z_i = \begin{cases} 1 & \text{Has consolidation} \\ 0 & \text{Otherwise} \end{cases}, \tag{3}$$

The object function was to minimize the following log-likelihood function:

$$\Theta_2 = \arg \min_{\Theta} -\sum_i \log P(z_i\mathbf{x}_i, \mathbf{f}(\mathbf{x}_i; \Theta)) \tag{4}$$

where $P(z_i\mathbf{x}_i, \mathbf{f}(\mathbf{x}_i; \Theta))$ is the probability that image i belongs to class z_i given the image $\mathbf{x}_i$ network output $\mathbf{f}(\mathbf{x}_i; \Theta)$. The exact formula of the probability function is not required.

The EM algorithm introduced a latent discrete variable $\mathbf{y} \in \{0,1\}^J$, which has meaning of pixelwise segmentation. Specifically, for pixel j:

$$y_j = \begin{cases} 1 & \text{Consolidation} \\ 0 & \text{Otherwise} \end{cases}. \tag{6}$$

For easier computation, the prior distribution of the image label z_i given image $\mathbf{x}_i$ and the latent variable $\mathbf{y}$ is considered to be pixelwise separable:

$$P(z_i|\mathbf{y}, \mathbf{x}_i) = c(z_i, \mathbf{x}_i) \prod_j \psi(z_i, y_j, x_{ij}), \tag{7}$$

where x_{ij} is the jth pixel in image $\mathbf{x}_i$; $c(z_i, \mathbf{x}_i)$ is a normalization factor so that $P(z_i|\mathbf{y}, \mathbf{x}_i)$ is a probability function, i.e.,

$$P(z_i = 0|\mathbf{y}, \mathbf{x}_i) + P(z_i = 1|\mathbf{y}, \mathbf{x}_i) = 1 \tag{8}$$

The basis function $\psi(z_i, y_j, x_{ij})$ is defined as:

$$\psi(z_i, y_j, x_{ij}) = \begin{cases} \phi(z_i, x_{ij}), & y_j = 1 \\ 1 - \phi(z_i, x_{ij}), & y_j = 0 \end{cases}. \tag{9}$$

For the conciseness of the paper, we will directly give the final equations for the EM algorithm here. Detailed derivation can be found in the appendix as well as in [31]. The EM algorithm iteratively alternates between the following Expectation (E) and Maximization (M) steps:

E-Step: given network parameter Θ' from the previous iteration, the latent variable $\mathbf{y}$ is solved pixelwise under the hard-EM approximation (using max instead of mean):

$$y_{ij} = \begin{cases} 1 & f_j(x_i; \Theta') + \phi(z_i, x_{ij}) > 1 \\ 0 & \text{Otherwise} \end{cases}, \tag{10}$$

where y_{ij} is the jth pixel of $\mathbf{y}_i$, which is the optimized latent variable for sample i. $f_j(x_i; \Theta')$ is the output of the current network at the jth pixel.

M-step: The network parameter Θ is optimized using the smooth Dice loss (2) by replacing the labels $\mathbf{l}_i$ with $\mathbf{y}_i$:

$$\Theta^* = \arg \min_{\Theta} -\frac{1}{N} \sum_i \frac{2\mathbf{y}_i \cdot \mathbf{f}(\mathbf{x}_i; \Theta) + \sigma}{\|\mathbf{y}_i\|_1 + \|\mathbf{f}(\mathbf{x}_i; \Theta)\|_1 + \sigma}. \tag{11}$$

D. Prior Modeling for Consolidation

The key to the success of EM algorithm is the choice of prior probability model $\phi(z_i, x_{ij})$ in (9). One choice of ϕ is to use a constant bias [31] for all the pixels according to the image-level

TABLE I
EM TRAINING ALGORITHM

Algorithm 1. EM Training of UNet-2.

INPUT $\mathbf{x}_i$, $\mathbf{z}_i$, infected region $\mathbf{m}_i$ predicted from UNet-1.
INITIALIZATION $\Theta \leftarrow \Theta_1$ from UNet-1.

1   WHILE not stopped:
2   Get a minibatch;
    E-step:
3   FOR i in the minibatch:
4       $\mathbf{f}_i \leftarrow \mathbf{m}_i \mathbf{f}(\mathbf{x}_i; \Theta)$, consolidation prediction;
5   FOR each pixel j:
6         $\phi_{ij} \leftarrow \mathbf{m}_i \phi(z_i, x_{ij})$, posterior probability;
7   IF $f_{ij} + \phi_{ij} > 1$ THEN $y_{ij} = 1$ ELSE $y_{ij} = 0$;
    M-step:
8   Compute $\nabla_\Theta \sum_i \text{Smooth\_Dice}\big(\mathbf{y}_i, \mathbf{m}_i \mathbf{f}(\mathbf{x}_i; \Theta)\big)$ and update Θ.

RETURN $\Theta_2 \leftarrow \Theta$.

TABLE II
DATASET INFORMATION

Hospital	# CT images	# Semantic labels
Firoozgar Hospital, Tehran, Iran (Training)	87	87
Shahid Beheshti Hospital, Kashan, Iran (Testing)	8	8
Massachusetts General Brigham, Boston, United States (Testing)	18	18
Yeungnam University Hospital, Gyeongsan, South Korea (Testing)	97	22
Azienda Ospedaliera Universitaria Maggiore della Carità, Novara, Italy (Testing)	15	14
MedSeg, Radiopaedia (Consolidation Testing)	9	9

label z_i:

$$\phi_1\left(z_i, x_{ij}\right) = \begin{cases} b_1, & z_i = 1 \\ 0, & z_i = 0 \end{cases}, \tag{12}$$

where $b_1 \in [0, 1]$ is the posterior probability of all pixels in image i being consolidation if consolidation presents.

However, (12) does not model any prior knowledge of consolidation into the model and the performance may be limited. It is known that consolidation usually has higher HU compared to GGO. Hence, we proposed the HU-based probability model as:

$$\phi_2\left(z_i, x_{ij}\right) = \begin{cases} \min\left(1, \frac{1}{1+\exp\{-k_2(x_{ij}-b_2)\}} + \frac{1}{2}\right), & z_i = 1 \\ 0, & z_i = 0 \end{cases}, \tag{13}$$

where k_2 and b_2 are hyperparameters to control the probability model. The probability of pixel j being consolidation increases with its HU value. When $x_{ij} \geq b_2$, $\phi_2\left(1, x_{ij}\right) = 1$, which means that the pixel must be consolidation. k_2 controls how steep the function increases. Larger k_2 will make the function closer to a step function. There is also an offset of 0.5 to the Sigmoid function, which means that for images with label 1, all the pixels were considered to have at least half chance of being consolidation. Another reason to add this 0.5 bias was that according to [31], the posterior probability function should bias towards foreground (consolidation), otherwise it may suffer from underestimation.

The overall training algorithm is given in Table I. We constrained the consolidation region within the infected region $\mathbf{m}_i \in \{0, 1\}^J$ predicted by UNet-1. The algorithm can be easily implemented based on the supervised learning framework. The only difference compared to a supervised training framework is the estimation of training label $\mathbf{y}_i$ at each iteration. The estimation was done in the E-step (steps 3-7). The training images first went through the network to generate predictions $\mathbf{f}_i$; then it was combined with the posterior probability ϕ to generate the training label $\mathbf{y}_i$ for the M-step. The M-step can be

implemented using standard network training algorithms such as the Adam optimizer [35].

E. Severity and Consolidation Quantification

The severity and consolidation quantifications are given as:

$$\text{severity score} = \frac{\text{area of infected region}}{\text{area of lung}}, \tag{14}$$

and

$$\text{consolidation score} = \frac{\text{area of consolidation}}{\text{area of lung}}. \tag{15}$$

III. EXPERIMENTAL SETUPS

A. Dataset

This study was approved by the respective Institutional Review Boards (IRBs) at Massachusetts General Brigham under protocol number 2020P000819 and 2016P000767. Informed consent forms were waived due to the retrospective nature of this study. The dataset consists of 225 unenhanced CT examinations of RT-PCR assay positive COVID-19 patients performed between January 1, 2020 and March 30, 2020, from various hospitals in Iran, Italy, South Korea, and the United States. The chest CT examinations were acquired on 6-256 slice multidetector-row scanners from three CT vendors (GE Healthcare, Waukesha, Wisconsin, US; Philips Healthcare, Eindhoven, The Netherlands; Siemens Healthineers, Forchheim, Germany). To validate the segmentation of consolidation regions, we also incorporated a public dataset from MedSeg,[3] where 9 CT images from Radiopeadia were annotated for regions of GGO and consolidation. A summary of the datasets is given in Table II. All the images were resampled to 256×256 resolution in the axial plane. If an image has a slice thickness thinner than 4 mm, it was resampled to 5 mm.

---

[3]http://medicalsegmentation.com/covid19/

Among the 225 CT images from our dataset, 149 were annotated for infected regions by two post-doctoral research fellows (with 1-2 years of experience in chest CT research), under the supervision of a subspecialty chest radiologist (13 years of clinical experience in thoracic imaging). The MedSeg dataset consists of 9 CT images from Radiopaedia with 829 slices in total. A radiologist segmented GGO and consolidation for each slice.

There were 22 out of 97 patients with semantic infection labels for the South Korean dataset. These 22 patients were randomly chosen before the development of the network. Annotating only part of the 97 patients saved valuable manual efforts due to the extensive works needed for the semantic annotation. The current testing dataset provided more than 7000 2D slices in total which is comparable to some of the existing studies [28]. A valid verification of UNet-1 was also reached with small p-value for the Pearson correlation between predicted and annotated infection areas. It also led to a more balanced testing dataset across different sites, so that the evaluation of UNet-1 will not be dominated by one single site.

The infection segmentation network (UNet-1) was trained on the images from Firoozgar Hospital (80 training and 7 validation) and tested on the 62 images with annotated infection areas from the other hospitals in our dataset.

To train the consolidation segmentation network (UNet-2), 19 patients from Firoozgar Hospital were confirmed by radiologists if the patient has only GGO or has both GGO and consolidation (15 had only GGO and 4 had both GGO and consolidation). UNet-2 was further validated on the MedSeg dataset to evaluate the accuracy of consolidation segmentation compared to the radiologist's annotation. It was also validated on the 138 testing CT images, where the prediction from UNet-2 was compared to the radiology reports. The patients were grouped to consolidation and non-consolidation groups using keywords including "consolidation" and "consolidated". The consolidation scores (15) were calculated for each patient and statistical testing was done between the two groups.

B. Parameters

Both UNet-1 and UNet-2 have 5 down-sampling blocks and 4 up-sampling blocks. Each block consists of two convolution layers with batch normalization and leaky ReLU activation. The number of channels after the first convolutional layer is 32. The number of channels was doubled after each down-sampling block and halved before each up-sampling block. Stride-two and transposed convolutions were employed for down-sampling and up-sampling, respectively. Concatenation between encoder and decoder paths were replaced by adding operation to reduce training parameters. The output layer is a 1×1 convolution layer with 1-channel output and Sigmoid activation.

Both networks take 7 consecutive axial slices as the input and output the segmentation map of the central slice. The value in the images was normalized to $(\mathrm{HU} + 1024)/110$ before being fed into the network. Various random transforms including rotation, translation, zooming, and flipping were incorporated during the training.
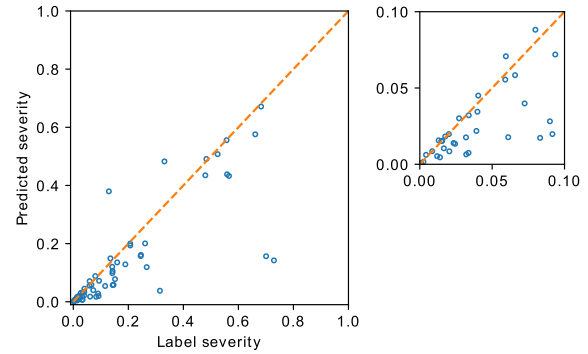

Fig. 2. Severity based on manual segmentation (label severity) versus the predicted severity. The orange line plotted the ideal prediction curve where the predicted severity score equals to the labelled severity score. Label severity between [0, 0.1] is shown in the zoom-in plot.

UNet-1 was trained on batches of 16 by the Adam algorithm for 200 epochs in total. The learning rate is 10^{-2}, 10^{-3} and 10^{-4} for epoch 1-50, 50-100, and 100-200.

UNet-2 was initialized from UNet-1 and trained with batch size of 16. Adam algorithm was used in the M-step. 50 epochs were trained with learning rate of 0.0005. We implemented both ϕ_1 and ϕ_2 as in (12) and (13) as the prior function and tried various hyperparameters b_1, b_2 and k_2. For ϕ_1, $b_1 = 1$ achieved the best Dice coefficient on the MedSeg dataset, which is equivalent to setting all the pixels in images with consolidation to consolidation. For ϕ_2, $b_2 = 9$, $k_2 = 0.5$ achieved the best Dice. $b_2 = 9$ is equivalent to -34 HU before the gray value normalization.

We also implemented thresholding as the baseline method [25], where pixels larger than -200 HU inside the predicted infected region were considered as consolidation.

C. Metrics

Performance of UNet-1 was evaluated on the 62 testing images by both the Dice coefficient and severity score defined in (14) compared to the radiologists' annotation.

For UNet-2, the segmentation performance was evaluated on the 9 CT images from MedSeg dataset with the Dice coefficients. The pixelwise true positive and false positive rate were also calculated inside the predicted infected regions. It was also evaluated on the 138 testing CT images to distinguish consolidation and non-consolidation groups using the consolidation score defined in (15).

IV. RESULTS

A. Severity Segmentation

The severity quantification results are given in Fig. 2. A Pearson correlation coefficient of $r = 0.825 \ (p < 0.001)$ was achieved between the predicted and the labelled severity score. A mean Dice coefficient of 0.632 was achieved with the segmentation network, which was comparable to the value reported in [28]. A reasonable performance of UNet-1 is necessary since it
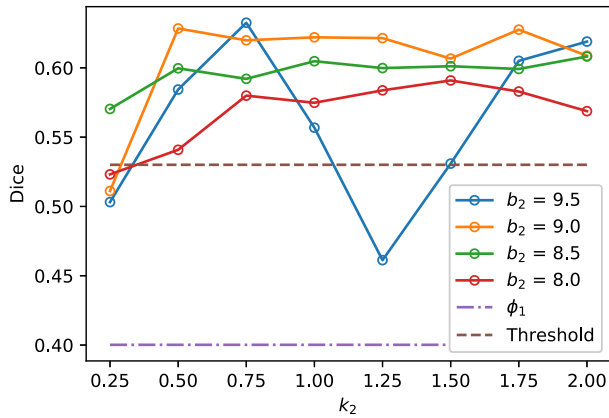
Fig. 3. The Dice coefficient on the MedSeg dataset with different b_2 and k_2. The solid lines with hollow points show the results with prior function ϕ_2. The purple dash-dotted line is the result from ϕ_1 with $b_1 = 1$. The brown dashed line is the result from the thresholding with -200 HU. The b_2 values 9.5, 9.0, 8.5, 8.0 correspond to 21, -34, -89, and -144 HUs respectively.
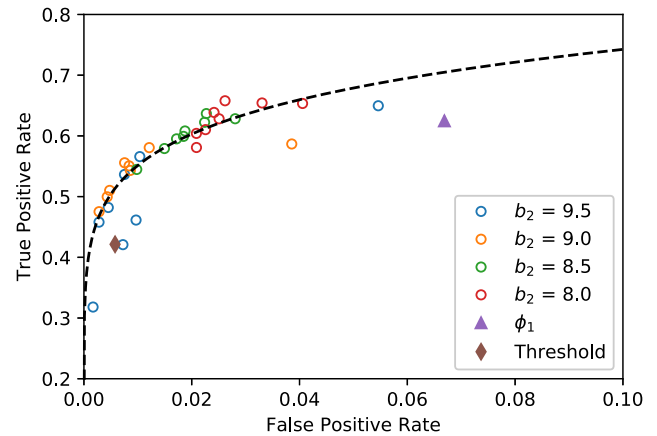

Fig. 4. The TPR and FPR trade-offs on the MedSeg dataset. Black dashed line is a ROC fitted from results of UNet-2 with ϕ_2 using different b_2 and k_2. Exponential function $TPR = FPR^\gamma$ was used for the ROC fitting.

provided the essential basis for the following weakly supervised learning of the consolidation segmentation.

B. Consolidation Segmentation

Fig. 3 shows the Dice coefficient of UNet-2 with ϕ_1 and ϕ_2 and the thresholding method on the MedSeg testing images. Thresholding by -200 HU could achieve a mean Dice coefficient of 0.530 of the consolidation regions. UNet-2 with ϕ_1 alone achieved a poor Dice coefficient of 0.400, which indicates that ϕ_1 cannot efficiently extract features of consolidation from the weak labels. The proposed prior function ϕ_2 increased the Dice coefficient to 0.628 with $b_2 = 9.0$ and $k_2 = 0.5$. The Dice coefficient generally increases with larger b_2 and keeps stable regarding k_2. However, the performance with $b_2 = 9.5$ becomes not very stable.

The trade-off between the true positive rate (TPR) and false positive rate (FPR) with different parameters are given in Fig. 4. The thresholding method will underestimate the consolidation regions, with a good specificity but relatively low sensitivity (TPR = 0.421, FPR = 0.006). EM algorithm with ϕ_1 will overestimate the consolidation, with a higher sensitivity but low specificity (TPR = 0.624, FPR = 0.067). EM algorithm with ϕ_2 at $b_2 = 9.0$ and $k_2 = 0.5$ had TPR = 0.555 and FPR = 0.008. A receiver operator curve (ROC) was fitted by exponential function for all the data points from ϕ_2 and is plotted as the black dashed line in Fig. 3. It can be observed that EM algorithm with the proposed ϕ_2 has better TPR-FPR trade-off compared to both thresholding and ϕ_1. Increasing b_2 will reduce the FPR but also reduce the TPR. This is because that larger b_2 raises the threshold of consolidation in ϕ_2 and the latent labels $\mathbf{y}_i$ will bias towards GGO.

Fig. 5 shows two slices of testing images from the MedSeg dataset with the GGO and consolidation segmentation overlay. The MedSeg dataset had very detailed annotation where the vessels were excluded from the GGO. However, in the training dataset our annotation did not particularly excluded the vessels. Hence, the predicted infected regions (green lines) did not exclude the vessels as the annotation.

It can be observed from Fig. 5 that thresholding significantly underestimated the consolidations compared to the annotations. The predicted consolidation regions are also very scattered. Meanwhile, ϕ_2 can generate continuous regions of consolidation that looks similar to the radiologists' annotation, whereas ϕ_1 generally failed to stably predict the consolidation regions.

Fig. 5 also demonstrates that thresholding and ϕ_2 have different source of false positive (FP). The FP of thresholding mostly comes from the vessels which have higher HU compared to lung tissue. The FP of ϕ_2 mostly comes from errors on the consolidation boundaries. To further verify this, we dilated the annotations with different dilation rates (0 to 9 pixels) and calculated the FPR at each dilation rate. The results are shown in Fig. 6. The FPR of both thresholding and ϕ_2 decreased with the increasing dilation rate. However, FPR of ϕ_2 decreased much more than thresholding, and it was less than the FPR of thresholding for all the dilation rates larger than 0. This indicates that the FP pixels of ϕ_2 are closer to the labels compared to thresholding. These pixels are usually because of the slight errors on the boundaries of the same region, rather than segmentation of an incorrect region.

It is also worth noticing that thresholding method with -200 HU as the threshold has already generated many FPs on the vessels. Further reducing the threshold may improve the TPR by including more pixels near the consolidation, but it will further deteriorate the FPR by including more vessels as consolidation.

C. Statistical Testing of Consolidation Score

The 138 testing patients were divided into consolidation and non-consolidation groups according to their radiology reports. Fig. 7 shows the box plot of the consolidation score predicted by UNet-2 with ϕ_2. The two groups were significantly different, with median value of 0.0403 versus 0.0043, and p-value of 2×10^{-9} under Mann-Whitney U test.
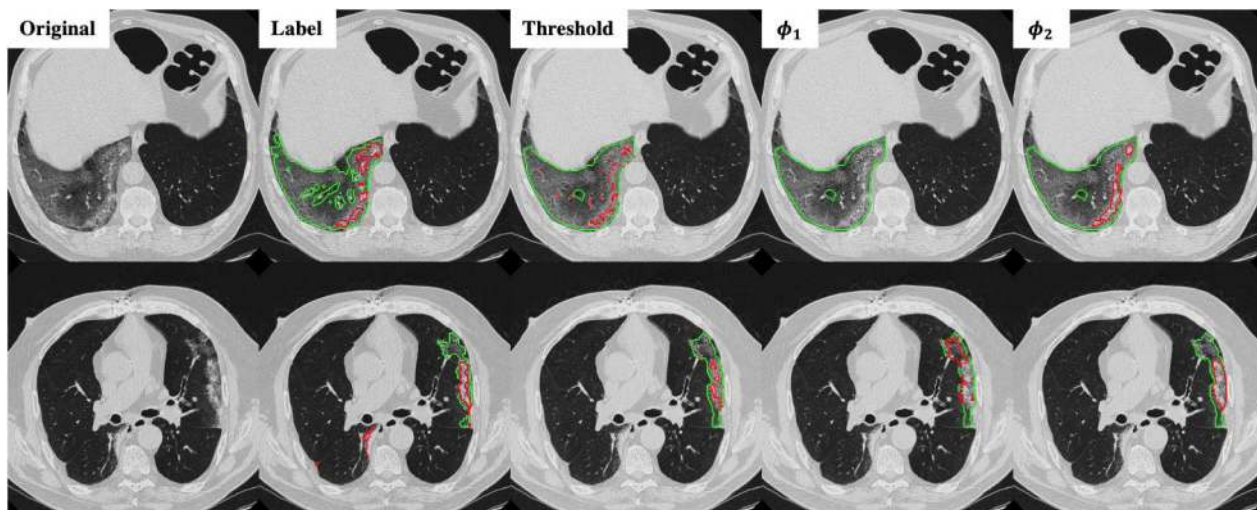
Fig. 5. Infection and consolidation segmentation results on the MegSeg dataset for two different slices. Green lines show the boundary of GGO and read lines show the boundary of consolidation.
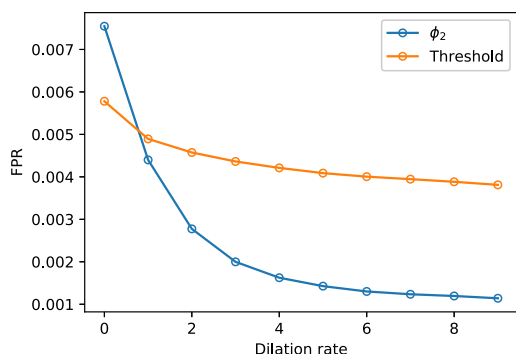

Fig. 6. The FPR of thresholding and EM with ϕ_2 ($b_2 = 9.0$, $k_2 = 0.5$) changing with different dilation rates of the labels.
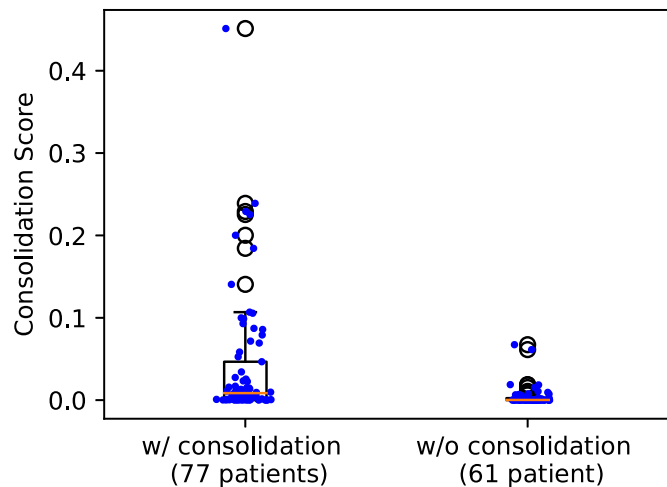

Fig. 7. Box plot of the consolidation scores in the consolidation and non-consolidation groups. Blue dots show individual data points' consolidation scores.

Most non-consolidation patients received lower consolidation scores when compared to patients with consolidation ($p < 0.0001$). There were two outliers which shows dramatically higher consolidation scores compared to the rest images in the non-consolidation group. Further investigation shows that these two images were overestimated because of the interlobular septal thickening, which had relatively higher HU compared to GGO. UNet-2 misclassified them into consolidation due to lack of training samples with interlobular septal thickening. As compared to groundglass opacities, both crazy-paving (groundglass opacities + septal thickening) and consolidation represent more advanced and severe disease, and therefore, this misclassification does not necessarily represent limitation of our algorithm.

V. DISCUSSION

In this work, we proposed a deep learning method to predict the infection and consolidation regions of the COVID-19 pneumonia based on chest CT. It demonstrated improved segmentation of consolidation compared to the thresholding method [25] and EM training without the prior model [31].

The main contribution of this work is the combination of pixel-level labels with patient-level type information through the proposed hybrid weak label-based training. A novel prior function ϕ_2 was proposed for the segmentation of consolidation in the EM framework. By incorporating the prior knowledge that consolidation usually has higher HU value into ϕ_2, the proposed network achieved improved performance compared to thresholding method and EM without such a prior. The proposed method also showed robustness for data coming from different sources, international sites, and protocols.

Although UNet-1 performs a standard segmentation task and is trained in a conventional supervised manner, a good performance is still crucial because UNet-1 is the basis for the following consolidation segmentation. UNet-1 also provides the

total infected region to calculate the severity score (14), which is clinically important for the estimation of the lung function. According to Fig. 2, the predicted scores were underestimated compared to the label. One of the main causes is that the model tends to miss regions with very mild GGO infections, which are not very different from normal lung tissue. Furthermore, the annotations also tend to dilate from the visible boundaries of GGO. Meanwhile, the model predictions are closer to the boundaries, leading to smaller regions compared to the annotation.

We used the EM algorithm as the framework for the weakly labeled training. From the derivation of section C-2, the proposed prior function ϕ_2 has clear physical meaning that it is the probability of a pixel belonging to consolidation given its pixel value and the image label, which was modeled by a Sigmoid function. We used $b_2 = 9.0$ as the parameter of choice for ϕ_2, which means that pixels larger than -34 HU inside the infected regions were considered as consolidation, and the pixels whose value were closer to -34 HU were considered to have higher probability of being consolidation.

It was found that further increasing the threshold b_2 to 9.5 led to instable performance regarding k_2. Further inspection showed that at $b_2 = 9.5$, $k_2 = 1.25$ the model had low sensitivity and only included the densest consolidations. The most possible reason is that $b_2 = 9.5$ corresponds to 21 HU, which is higher than most consolidation pixels. When k_2 is small, the difference on ϕ_2 between less dense and denser consolidations is not too large, and less dense consolidations could be included into the latent label $\mathbf{y}$. When k_2 is large, ϕ_2 becomes very steep and since most consolidation pixels are below the changing point b_2, the difference between their weights is small, which leads to similar weights between less dense and denser consolidations. However, when k_2 is at a certain value, the denser consolidations have considerably larger weights than the less dense ones. In consequence, only very dense consolidations are considered which leads to the low sensitivity and Dice.

Currently the thresholding method is considered as a reliable method to separate GGO and consolidation [25]. We also observed a good Dice coefficient using thresholding only compared to the proposed weakly labeled learning. However, further investigation found that thresholding tends to misclassify vessels inside the infected regions to consolidation, as they have higher HU compared to GGO and other lung tissues. Most of the FPs in thresholding results came from these vessels, which are far from real consolidation regions. Although the proposed approach had similar FPR compared to thresholding, these FPs are mostly from difference between the boundaries of the labeled and predicted consolidation.

We believe that deep learning-based quantification can help address the need in patients with worsening respiratory status and moderate or severe infection where chest CT scan is recommended, and often performed [8]. The developed deep learning-based CT segmentation can serve as an important tool to help assess disease severity and progression as well as to predict prognosis. The predicted severity score of COVID-19 pneumonia along with other clinical and laboratory markers such as patient age, comorbidities, and oxygen saturation can help caretaking physicians determine patients in need of intubation or ICU admission. Although there are no known and approved treatment for COVID-19 pneumonia, multiple, ongoing clinical trials involving antiviral agents and antibodies can benefit from the proposed method which helps quantify the disease burden and thus, assess disease response or progression in an objective manner. Consistent scoring facilitated by the developed automatic tool can empower both cross-sectional and longitudinal comparisons, enable us better to understand the populational characteristics and the temporal evolution of the COVID-19 disease.

The proposed method has the benefit of segmenting consolidation regions without additional efforts to semantically annotate them on the CT images. Despite the limited number of weakly-labeled patients used to train the consolidation network, the network demonstrated promising performance on the MedSeg testing dataset which came from different sources with the training data. It can be used alone or combined with semantic labels for semi-supervised learning [28]. Inclusion of weakly labeled data can significantly increase the number of training data and generalizability to different protocols. The proposed method may also be applied to segmentation tasks beyond pulmonary consolidations, as long as the target has pixelwise features that can be modeled, e.g., higher/lower pixel values compared to the background.

VI. CONCLUSION

In this work we have proposed a deep learning method for infection and consolidation segmentation from CT images based on hybrid week labels. The network was initially trained with single-class contours and fine-tuned through weak patient-level labels. Evaluations based on datasets from multiple hospitals across the world demonstrate the effectiveness of the proposed framework. Future work will focus on more evaluations and score calculation for other infection types.

APPENDIX

Here we give the detailed derivation of the EM algorithm (10) and (11). Compared to the original EM framework [30], our derivation supplemented some details such as the existence of the pixelwise separable basis ϕ is (7).

Given UNet-2 $\mathbf{f}(\mathbf{x}; \Theta)$ and the image labels z_i, we aim to minimize the following log-likelihood function

$$\Theta_2 = \arg \min_{\Theta} - \sum_i \log P\left(z_i \mathbf{x}_i, \mathbf{f}\left(\mathbf{x}_i; \Theta\right)\right) \quad (16)$$

The following equation always holds regardless of the choice of the latent variable $\mathbf{y}$:

$$P\left(z_i \mathbf{x}_i, \mathbf{f}\left(\mathbf{x}_i; \Theta\right)\right)$$
$$= \sum_{\mathbf{y}} P\left(z_i | \mathbf{y}, \mathbf{x}_i, \mathbf{f}\left(\mathbf{x}_i; \Theta\right)\right) P\left(\mathbf{y} | \mathbf{x}_i, \mathbf{f}\left(\mathbf{x}_i; \Theta\right)\right) \quad (17)$$

Here we selected $\mathbf{y} \in \{0, 1\}^J$ as in (6) with the following two assumptions:

First, $\mathbf{y}$ connects z_i and $\mathbf{f}(\mathbf{x}_i; \Theta)$:

$$P\left(z_i | \mathbf{y}, \mathbf{x}_i, \mathbf{f}\left(\mathbf{x}_i; \Theta\right)\right) = P\left(z_i | \mathbf{y}, \mathbf{x}_i\right); \quad (18)$$

Second, $\mathbf{f}(\mathbf{x}_i; \Theta)$ connects $\mathbf{x}_i$ and $\mathbf{y}$:

$$P(\mathbf{y}|\mathbf{x}_i, \mathbf{f}(\mathbf{x}_i; \Theta)) = P(\mathbf{y}|\mathbf{f}(\mathbf{x}_i; \Theta)). \quad (19)$$

Substitute (18) and (19) into (17) and we have:

$$P(z_i \mathbf{x}_i, \mathbf{f}(\mathbf{x}_i; \Theta)) = \sum_{\mathbf{y}} P(z_i|\mathbf{y}, \mathbf{x}_i) P(\mathbf{y}|\mathbf{f}(\mathbf{x}_i; \Theta)). \quad (20)$$

EM algorithm is essentially following the optimization transfer principle [36]. In the E-step, which builds a surrogate function of the original problem (16). The surrogate is then optimized during the M-step. E-step builds the surrogate function $Q_1(\Theta\Theta')$ by taking the expectation of the log likelihood $\log P(\mathbf{y}, z_i|\mathbf{x}_i, \mathbf{f}(\mathbf{x}_i; \Theta))$ [37] as:

$$Q_1(\Theta|\Theta') = -\sum_i \sum_{\mathbf{y}} P(\mathbf{y}|z_i, \mathbf{x}_i, \mathbf{f}(\mathbf{x}_i; \Theta'))$$
$$\times \log P(\mathbf{y}, z_i|\mathbf{x}_i, \mathbf{f}(\mathbf{x}_i; \Theta)), \quad (21)$$

where Θ' is the network parameters from the previous iteration. According to (18) and (19), the joint distribution can be written as:

$$\log P(\mathbf{y}, z_i|\mathbf{x}_i, \mathbf{f}(\mathbf{x}_i; \Theta))$$
$$= \log P(\mathbf{y}|\mathbf{x}_i, \mathbf{f}(\mathbf{x}_i; \Theta)) + \log P(z_i|\mathbf{y}, \mathbf{x}_i, \mathbf{f}(\mathbf{x}_i; \Theta))$$
$$= \log P(\mathbf{y}|\mathbf{f}(\mathbf{x}_i; \Theta)) + \log P(z_i|\mathbf{y}, \mathbf{x}_i). \quad (22)$$

Substitute (22) into (21) and remove all the terms irrelevant to Θ, the surrogate function becomes:

$$Q_2(\Theta\Theta') = -\sum_i \sum_{\mathbf{y}} P(\mathbf{y}|z_i, \mathbf{x}_i, \mathbf{f}(\mathbf{x}_i; \Theta'))$$
$$\times \log P(\mathbf{y}|\mathbf{f}(\mathbf{x}_i; \Theta)). \quad (23)$$

Because summation over all possible $\mathbf{y}$ is not practical, the hard-EM approximation was taken, where the single point $\mathbf{y}$ which maximizes $P(\mathbf{y}|z_i, \mathbf{x}_i, \mathbf{f}(\mathbf{x}_i; \Theta'))$ was taken instead of the expectation. Denote $\mathbf{y}_i$ as the $\mathbf{y}$ that maximize the probability for image i. It can be calculated as:

$$\mathbf{y}_i = \arg\max_{\mathbf{y}} \log P(\mathbf{y}|z_i, \mathbf{x}_i, \mathbf{f}(\mathbf{x}_i; \Theta'))$$

$$= \arg\max_{\mathbf{y}} \log \frac{P(z_i|\mathbf{y}, \mathbf{x}_i, \mathbf{f}(\mathbf{x}_i; \Theta')) P(\mathbf{y}|\mathbf{x}_i, \mathbf{f}(\mathbf{x}_i; \Theta'))}{P(z_i|\mathbf{x}_i, \mathbf{f}(\mathbf{x}_i; \Theta'))}$$

$$= \arg\max_{\mathbf{y}} \log P(z_i|\mathbf{y}, \mathbf{x}_i) + \log P(\mathbf{y}|\mathbf{f}(\mathbf{x}_i; \Theta')), \quad (24)$$

where in the last equality, the term without $\mathbf{y}$ was dropped, and equations (18) and (19) were used to remove $\mathbf{f}(\mathbf{x}_i; \Theta')$ in the first term and $\mathbf{x}_i$ in the second term, respectively.

According to the definition of $\mathbf{y}$ in (6), $P(\mathbf{y}|\mathbf{f}(\mathbf{x}_i; \Theta'))$ should be pixelwise separable, leading to:

$$\log P(\mathbf{y}|\mathbf{f}(\mathbf{x}_i; \Theta')) = \sum_j \log P(y_j|f_j(\mathbf{x}_i; \Theta')). \quad (25)$$

For the prior distribution $P(z_i|\mathbf{y}, \mathbf{x}_i)$, according to Bayes' theorem, we have:

$$P(z_i|\mathbf{y}, \mathbf{x}_i) = \frac{P(\mathbf{y}, \mathbf{x}_i|z_i) P(z_i)}{P(\mathbf{y}, \mathbf{x}_i)}. \quad (26)$$

By modeling the joint (conditional) distributions as independent pixelwise, we have:

$$P(z_i|\mathbf{y}, \mathbf{x}_i) = \frac{P(z_i) \prod_j P(y_j, x_{ij}|z_i)}{\prod_j P(y_j, x_{ij})}$$
$$= P(z_i) \prod_j \frac{P(y_j, x_{ij}|z_i)}{P(y_j, x_{ij})}$$
$$= P(z_i) \prod_j \psi_0(z_i, y_j, x_{ij}). \quad (27)$$

ψ in (9) can be derived from ψ_0 by multiplying proper normalization factors. Let

$$\psi(z_i, y_j, x_{ij}) = \frac{\psi_0(z_i, y_j, x_{ij})}{\psi_0(z_i, 1, x_{ij}) + \psi_0(z_i, 0, x_{ij})}, \quad (28)$$

and ψ will satisfy the sum-to-one requirement in (9). Substitute (28) into (27) and we will reach

$$P(z_i|\mathbf{y}, \mathbf{x}_i) = P(z_i) \prod_j [\psi_0(z_i, 1, x_{ij}) + \psi_0(z_i, 0, x_{ij})]$$
$$\times \prod_j \psi(z_i, y_j, x_{ij})$$
$$= c(z_i, \mathbf{x}_i) \prod_j \psi(z_i, y_j, x_{ij}) \quad (29)$$

which gives equation (7).

Substitute (25) and (29) into (24) and remove the terms not relevant to $\mathbf{y}$, we can get the separable distribution to be maximized as:

$$\mathbf{y}_i = \arg\max_{\mathbf{y}} \sum_j \log P(y_j f_j(\mathbf{x}_i; \Theta')) \psi(z_i, y_j, x_{ij}), \quad (30)$$

which can be solved pixelwise as

$$y_{ij} = \arg\max_{y_j} P(y_j f_j(\mathbf{x}_i; \Theta')) \psi(z_i, y_j, x_{ij}). \quad (31)$$

After $\mathbf{y}_i$ is solved, the hard-EM approximation of (23) becomes:

$$Q(\Theta\Theta') = -\sum_i \log P(\mathbf{y}_i|\mathbf{f}(\mathbf{x}_i; \Theta)), \quad (32)$$

which is the final surrogate function from the E-step of the EM algorithm. Minimization of $Q(\Theta|\Theta')$ leads to the M-step given in (11).

To solve (31), denote $f_{ij} = f_j(\mathbf{x}_i; \Theta')$ and $\phi_{ij} = \phi(z_i, x_{ij})$, we have

$$P(y_j f_j(\mathbf{x}_i; \Theta')) = \begin{cases} f_{ij}, & y_j = 1 \\ 1 - f_{ij}, & y_j = 0 \end{cases}, \quad (33)$$

and

$$\psi(z_i, y_j, x_{ij}) = \begin{cases} \phi_{ij}, & y_j = 1 \\ 1 - \phi_{ij}, & y_j = 0 \end{cases}. \quad (34)$$

Note that (34) is the same with (9). The joint probability function becomes:

$$P(y_j f_j(\mathbf{x}_i; \Theta')) \psi(z_i, y_j, x_{ij})$$
$$= \begin{cases} f_{ij}\phi_{ij}, & y_j = 1 \\ (1 - f_{ij})(1 - \phi_{ij}), & y_j = 0 \end{cases} \quad (35)$$

Hence, the solution to (31) is:

$$y_{ij} = \begin{cases} 1 & f_{ij}\phi_{ij} > (1 - f_{ij})(1 - \phi_{ij}) \\ 0 & \text{Otherwise} \end{cases}. \qquad (36)$$

Because $(1 - f_{ij})(1 - \phi_{ij}) = 1 - f_{ij} - \phi_{ij} + f_{ij}\phi_{ij}$, (36) can be further reduced to:

$$y_{ij} = \begin{cases} 1 & f_{ij} + \phi_{ij} > 1 \\ 0 & \text{Otherwise} \end{cases}, \qquad (37)$$

which is the same with the E-step given in (10).

REFERENCES

[1] E. Dong, H. Du, and L. Gardner, "An interactive web-based dashboard to track COVID-19 in real time," *Lancet. Infect. Dis.*, vol. 20, no. 5, pp. 533–534, May 2020.

[2] C. Huang *et al.*, "Clinical features of patients infected with 2019 novel coronavirus in wuhan, china," vol. 395, no. 10223, pp. 497–506, 2020.

[3] Y. Liu, A. A. Gayle, A. Wilder-Smith, and J. Rocklöv, "The reproductive number of COVID-19 is higher compared to SARS coronavirus," *J. Travel Med.*, vol. 27, no. 2, pp. 1–4, 2020.

[4] T. Ai *et al.*, "Correlation of chest CT and RT-PCR testing in coronavirus disease 2019 (COVID-19) in china: A report of 1014 cases," *Radiology*, vol. 296, no. 2, pp. E32–E40, 2020.

[5] Y. Fang *et al.*, "Sensitivity of chest CT for COVID-19: Comparison to RT-PCR," *Radiology*, vol. 296, no. 2, pp. E115–E117, 2020.

[6] J. P. Kanne, B. P. Little, J. H. Chung, B. M. Elicker, and L. H. Ketai, "Essentials for radiologists on COVID-19: An update—Radiology scientific expert panel," *Radiology*, vol. 296, no. 2, pp. E113–E114, 2020.

[7] Z. Wen *et al.*, "Coronavirus disease 2019: Initial detection on chest CT in a retrospective multicenter study of 103 chinese subjects," *Radiol., Cardiothoracic Imag.*, vol. 2, no. 2, 2020, Paper e200092.

[8] G. D. Rubin *et al.*, "The role of chest imaging in patient management during the COVID-19 pandemic: A multinational consensus statement from the Fleischner society," *Chest*, vol. 158, no. 1, pp. 106–116, Jul. 2020.

[9] E. Driggin *et al.*, "Cardiovascular considerations for patients, health care workers, and health systems during the COVID-19 pandemic," *J. Amer. College Cardiol.*, vol. 75, no. 18, pp. 2352–2371, 2020.

[10] F. Pan *et al.*, "Time course of lung changes on chest CT during recovery from 2019 novel coronavirus (COVID-19) pneumonia," *Radiology*, vol. 295, no. 3, pp. 715–721, Jun. 2020.

[11] M. Chung *et al.*, "CT imaging features of 2019 novel coronavirus (2019-nCoV)," *Radiology*, vol. 295, no. 1, pp. 202–207, 2020.

[12] Y. Li and L. Xia, "Coronavirus disease 2019 (COVID-19): Role of chest CT in diagnosis and management," *Amer. J. Roentgenol.*, pp. 1–7, 2020.

[13] H. Kim, "Outbreak of Novel Coronavirus (COVID-19): What is the Role of Radiologists?," *Eur. Radiol.*, vol. 30, no. 6, pp. 3266–3267, Jun. 2020.

[14] A. Krizhevsky, I. Sutskever, and G. E. Hinton, "Imagenet classification with deep convolutional neural networks," in *Proc. Adv. Neural Inf. Process. Syst.*, 2012, pp. 1097–1105.

[15] L. Li *et al.*, "Using artificial intelligence to detect COVID-19 and community-acquired pneumonia based on pulmonary CT: Evaluation of the diagnostic accuracy," *Radiology*, vol. 296, no. 2, pp. E65–E71, Aug. 2020.

[16] B. Wang *et al.*, "AI-assisted CT imaging analysis for COVID-19 screening: Building and deploying a medical AI system," *Appl. Soft Comput.*, Nov. 2020, Art. no. 106897.

[17] O. Gozes, M. Frid-Adar, N. Sagie, H. Zhang, W. Ji, and H. Greenspan, "Coronavirus detection and analysis on chest CT with deep learning," 2020, *arXiv:2004.02640*.

[18] O. Gozes *et al.*, "Rapid ai development cycle for the coronavirus (covid-19) pandemic: Initial results for automated detection & patient monitoring using deep learning ct image analysis," 2020, *arXiv:2003.05037*.

[19] J. Chen *et al.*, "Deep learning-based model for detecting 2019 novel coronavirus pneumonia on high-resolution computed tomography," *Sci. Rep.*, vol. 10, no. 1, 2020, Art. no. 19196.

[20] S. Hu *et al.*, "Weakly supervised deep learning for COVID-19 infection detection and classification from CT images," *IEEE Access*, vol. 29, no. 8, pp. 118869–118883, 2020.

[21] C. Zheng *et al.*, "Deep learning-based detection for COVID-19 from chest CT using weak label," medRxiv, 2020.

[22] S. Wang *et al.*, "A fully automatic deep learning system for COVID-19 diagnostic and prognostic analysis," *Eur. Respir. J.*, vol. 56, no. 2, Aug. 2020.

[23] L. Huang *et al.*, "Serial quantitative chest CT assessment of COVID-19: Deep-learning approach," *Radiol., Cardiothoracic Imag.*, vol. 2, no. 2, 2020, Paper e200075.

[24] F. Shan *et al.*, "Lung infection quantification of COVID-19 in CT images with deep learning," 2020, *arXiv:.04655*.

[25] S. Chaganti *et al.*, "Automated quantification of CT patterns associated with COVID-19 from chest CT," *Radiol. Artif. Intell.*, vol. 2, no. 4, Jul. 2020, Art. no. e200048.

[26] Z. Tang *et al.*, "Severity assessment of COVID-19 using CT image features and laboratory indices," *Phys. Med. Biol.*, Oct. 2020.

[27] R. Yang *et al.*, "Chest CT severity score: An imaging tool for assessing severe COVID-19," *Radiol., Cardiothoracic Imag.*, vol. 2, no. 2, 2020, Paper e200047.

[28] D.-P. Fan *et al.*, "Inf-Net: Automatic COVID-19 lung infection segmentation from CT images," *IEEE Trans. Med. Imag.*, vol. 39, no. 8, pp. 2626–2637, Aug. 2020.

[29] W. Zhu, Q. Lou, Y. S. Vang, and X. Xie, "Deep multi-instance networks with sparse label assignment for whole mammogram classification," in *Proc. Int. Conf. Med. Image Comput. Comput.-Assisted Intervention*, 2017, pp. 603–611.

[30] Y. Wei, H. Xiao, H. Shi, Z. Jie, J. Feng, and T. S. Huang, "Revisiting dilated convolution: A simple approach for weakly-and semi-supervised semantic segmentation," in *Proc. IEEE Conf. Comput. Vis. Pattern Recognit.*, 2018, pp. 7268–7277.

[31] G. Papandreou, L.-C. Chen, K. P. Murphy, and A. L. Yuille, "Weakly-and semi-supervised learning of a deep convolutional network for semantic image segmentation," in *Proc. IEEE Int. Conf. Comput. Vis.*, 2015, pp. 1742–1750.

[32] W. Zhu, Y. S. Vang, Y. Huang, and X. Xie, "Deepem: Deep 3d convnets with em for weakly supervised pulmonary nodule detection," in *Proc. Int. Conf. Med. Image Comput. Comput.-Assisted Intervention*, 2018, pp. 812–820.

[33] O. Ronneberger, P. Fischer, and T. Brox, "U-net: Convolutional networks for biomedical image segmentation," in *Proc. Int. Conf. Med. image Comput. Comput.-assisted intervention*, 2015, pp. 234–241.

[34] J. Hofmanninger, F. Prayer, J. Pan, S. Röhrich, H. Prosch, and G. Langs, "Automatic lung segmentation in routine imaging is primarily a data diversity problem, not a methodology problem," *Eur. Radiol. Exp.*, vol. 4, no. 1, p. 50, Dec. 2020.

[35] D. P. Kingma and J. Ba, "Adam: A method for stochastic optimization," in *Proc. 3rd Int. Conf. Learn. Representations (ICLR)*, San Diego, CA, USA, May 7–9, 2015.

[36] H. Erdogan and J. A. Fessler, "Monotonic algorithms for transmission tomography," *IEEE Trans. Med. Imag.*, vol. 18, no. 9, pp. 801–814, Sep. 1999.

[37] R. J. Little and D. B. Rubin, in *Statistical Analysis With Missing Data*. New York, NY, USA: John Wiley Sons, 2019.